Advances in Science and Technology Research Journal

Advances in Science and Technology Research Journal, 2026, 20(4), 60–75
https://doi.org/10.12913/22998624/214180
ISSN 2299-8624, License CC-BY 4.0

Received: 2025.09.22
Accepted: 2026.02.15
Published: 2026.03.01

Microstructure optimization of pantographic metamaterials through design and analysis

Rafał Drobnicki[1*], Yuriy Pyr'yev[1], Marek Pawlikowski[1]

[1] Faculty of Mechanical and Industrial Engineering, Warsaw University of Technology, Narbutta 85, 02-524 Warsaw, Poland
* Corresponding author's e-mail: rafal.drobnicki@pw.edu.pl

ABSTRACT

Pantographic metamaterials are lattices of beams arranged in two bias directions and joined by compliant pivots that act as rotational connectors. These pivots govern how unit cells of the lattice reorient and transmit load. Tailoring their rotational stiffness can reshape the mechanical response without changing the base material. This study investigates whether adjusting the rotational stiffness of pivots embedded in the microstructure of a pantographic metamaterial can lead to uniform spring work, reduce stress concentration, and improve macroscopic stability. The pantographic lattices are subjected to bias extension and shear tests and to a case with no external load, where an initial bending moment field is applied directly to the pivots. Their mechanical response is simulated using a discrete model of beams and springs in which the pivots are represented by translational-rotational springs. The simulations span three lattice refinements. Optimization consistently flattens the spring energy distribution, lowers peak von Mises stress and produces an interpretable stiffness distribution aligned with known pantographic mechanism: a narrowed, low-stress waist under bias extension and a diamond-shaped interior skeleton under shear. These improvements are achieved without sacrificing global stiffness. The results indicate that energy-equalizing stiffness fields can serve as a microstructural pre-conditioning strategy for damage mitigation and design transferability across scales.

Keywords: metamaterial, optimization, continuum mechanics, pantographic microstructure.

INTRODUCTION

The term "metamaterials" for that kind of materials which owe their unique properties to their specially designed internal physical structure rather than their chemical composition was first used by Rodger M. Walser in 1999 to distinguish materials with new and unconventional properties from those exhibiting conventional electromagnetic behavior [1,2]. Although they consist of individual components that mimic the behavior of atoms or molecules in natural materials, metamaterials exhibit macroscopic properties similar to those of a continuous substance [3,4]. As a result, their physical properties are not found in natural substances or traditional engineered materials.

Mechanical metamaterials have their origins in research on phononic crystals from the 1980s [5]. The structures of a mechanical metamaterial can be designed in all three dimensions, which allows for the modulation of various physical quantities through the combinatorial arrangement of various periodic and non-periodic geometric unit cells. Owing to its structural architecture, it exhibits dynamic and tunable mechanical responses to changing environmental conditions. Since the 1980s, advances in materials science, mechanics, and manufacturing technology have enabled the development of a wide range of applications for mechanical metamaterials, such as reducing vibration and noise, absorbing energy, reducing device weight, and increasing structural strength [6].

An interesting case of a mechanical metamaterial is a metamaterial with a pantographic microstructure. The term "pantographic" refers to the specific design of the microstructure, which consists of two orthogonal arrays of beams connected by internal cylinders that deform in a

specific direction while resisting deformation in other directions [7]. These metamaterials are an example of materials whose macroscopic continuous description necessitates second-gradient continuum model. This implies that traditional first-gradient continuum models are insufficient to fully describe the behavior of these materials, and higher-order models are required to capture their unique properties [8].

The first numerical simulation on pantographic structures dates back to 2014 and focused on simulations analyzing the propagation of waves in one-dimensional pantographic structures [9]. In 2015, the first experimental results were published, detailing BIAS extension tests performed on pantographic structures, thus providing insight into their mechanical behavior [10]. Experimental research has shown over the years that pantographic structures have several unusual properties. These include the ability to undergo large deformation while maintaining an elastic range, exhibiting high resistance to damage, maintaining stable macroscopic mechanical behavior despite small changes in microstructure and micromechanical properties, and exhibiting anisotropic behavior [11]. Due to their properties, pantographic structures hold significant potential for applications across various fields, including the aviation industry, robotics, civil engineering, and biomedical engineering [12,13].

The first attempt to model a metamaterial with a pantographic microstructure was undertaken in 2003. This attempt aimed to identify a micromodel that would enable obtaining the simplest model of the second-gradient as a result of the homogenization procedure [14]. Currently, the dominant modeling techniques include the discrete Hencky-type model for micro-scale applications [15], the nonlinear Euler-Bernoulli beam theory for meso-scale analysis [16] and the second-gradient homogenization model for macro-scale representation [15,17].

The present work adopts a meso-inspired discrete beam network representation, but with a different pivot modeling strategy. In conventional meso-scale model, pivots are implemented either as ideal hinges transmitting only translational constraints while allowing unrestricted rotation or as hinges complemented solely by a torsional spring, thus neglecting translational compliance. In this work, each pivot is realized as a kinematic hinge defined by displacement constraints, complemented with translational-rotational springs. This enables the simultaneous presence of rotational and translational flexibility, allowing coupling effects absent in classical meso-scale approaches. Furthermore, rotational stiffness is parametrically varied during simulations, enabling a transition from a highly compliant joint to an almost rigid connection. This enhanced pivot modelling provides a more realistic description of local kinematics.

Few studies [18,19] address the optimization of metamaterials with a pantographic microstructure despite their remarkable mechanical performance for specific load cases. In particular, the influence of microstructural geometry on the uniformity of elastic energy distribution and stress concentration reduction remains underexplored. The present paper focuses on modeling the microstructure of a mechanical metamaterial to achieve a uniform distribution of elastic energy and stiffness across individual microstructural elements. The optimization process sought to impart distinctive properties to the metamaterial, tailored for potential biomechanical applications. Among the key advantages of this process are the reduction of local stress, enhanced structural stability, and improved durability of the optimized microstructure.

MATERIALS AND METHODS

A discrete beam and spring representation was adopted for the pantographic metamaterial, including its geometries, microstructural refinements, and procedures for loading and optimization. The geometry and lattice are first described. Pivot modeling was implemented as a kinematic hinge complemented by translational-rotational springs, which served as the optimized element. Material data and boundary conditions are provided for the BIAS extension, shear, and pre-moment cases. An energy-equalizing stiffness redistribution algorithm is applied, based on a logarithmic multiplicative update scheme with a two-constraint projection and a based stopping rule with the corresponding numerical parameters provided in Table 2.

Geometric model

The specimen was designed with rectangular dimensions of $\mathbb{L}_1 = 0.07$ [m] × $\mathbb{L}_2 = 0.21$ [m]. The elongated aspect ratio of 1:3 was selected

Table 1. List of models with their corresponding number of hinges

N_f	7	10	14
Number of hinges	319	637	1229

by the necessity of observing global deformation mechanisms such as wave propagation, buckling and mode localization [9]. This choice of dimensions is also consistent with general homogenizations approaches for periodic media. The adoption of at least three-unit cells in shorter direction already provided size-independent result and is necessary to ensure that the mechanical response is not dominated by boundary effects. Increasing the number of unit cells in this direction does not qualitatively change the overall response but alters local aspect ratios [20]. The longer side of specimen contained more than a dozen unit cells, which made it possible to capture the anisotropy and dispersive phenomena characteristic of metamaterial with pantographic microstructure. Since these effects arise directly from the domain of the periodic microstructure, the specimen must be sufficiently long to accommodate several wavelengths within its domain [21,22]. This configuration was sufficient for the mechanical response to no longer depend significantly on domain enlargement. Increasing the number of unit cells in both directions did not change the metamaterial but brought its behavior closer to what it would be in a continuum material. The discrete model geometry was generated using Salome, an open-source software distributed under the GNU LGPL license. Figure 1 illustrates the discrete geometry of a pantographic metamaterial, composed of seven representative unit cells along the short side $\mathbb{L}_1$ and twenty-one along the long side $\mathbb{L}_2$.

The modeled specimens comprise seven-, ten-, and fourteen-unit cells along the short side, corresponding to twenty-one, thirty, and forty-two cells along the long side, respectively. In order to facilitate differentiation between the analyzed specimens, each model is identified by the number of unit cells along the short side.

As shown in Table 1, the number of hinges directly determines the number of springs subjected to the optimization process. Here, N_f denotes the number of unit cells along the short side $\mathbb{L}_1$.

Mechanical properties

In the continuous model as well as in the manufactured specimen, the pivots were implemented as cylindrical connections between beams. Commonly, either standard pivots or quasi-perfect pivots are employed. Figure 2b shows a quasi-perfect pivot, which in theory does not involve torsional energy. In the discrete model, the pivot was first introduced as kinematic hinge constraint. Certain translational degrees of freedom were eliminated between the nodes, while rotation was allowed. The kinematic condition itself only prescribes the relative motion of the nodes and does not impart

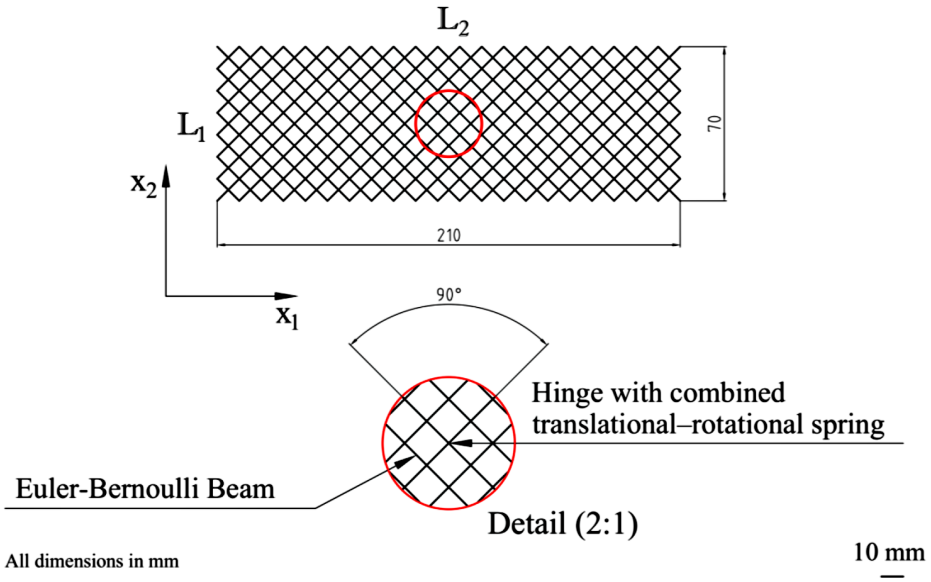

Figure 1. Discrete model of pantographic metamaterial. Overall size 70 × 210 mm, scale bar 10 mm, all dimensions in mm

any stiffness. Therefore, no energy is stored in the constraint. An additional translational-rotational spring was added to reproduce the torsional compliance of the cylindrical connectors through an equivalent stiffness k_r. As the rotational spring stiffness k_r increases, the pivot progressively approaches the behavior of a standard joint, as illustrated in Figure 2a.
The stiffness k_r is calculated as:

$$k_r = \frac{G \cdot J}{L} \tag{1}$$

where: G – the shear modulus, J – the polar moment of inertia of the cross-sectioned area, L – the height of the cylinder.

The beams dimension together with Equation 1 define the maximum admissible stiffness of the spring. In particular, the cylinder diameter used in the evaluation of J cannot exceed the beam width. The translational stiffness coefficients k were set to negligibly small values 10^{-9} $N{\cdot}m^{-1}$ in order to avoid numerical singularities. Since the translational degrees of freedom were already constrained by the kinematic hinge definition, these values did not influence the mechanical response of the system. The rotational stiffness coefficient k_r were set to 0.025519 $N{\cdot}m{\cdot}rad^{-1}$, which corresponds approximately to a pivot of 0.0008 m in a diameter and 0.001 m in height. The beams were modeled as linear elastic, isotropic, and homogenous, with a Young's modulus E = 1650 MPa and a Poisson's ratio of $\upsilon = 0.3$. These values correspond to the typical mechanical properties of additively manufactured polyamide PA12 specimen reported in [18], which is consistent with the material used for the physical prototypes. At the same time, both the width and the height of the beam cross-section were set to 0.001 m.

Numerical implementation

Finite element simulations were performed with Code_Aster v14.6, an analysis package that uses Fortran, Python and C^{++}. Inputs included an ASCII command file, the finite element mesh and a parameter file defining the analysis parameters. The BIAS extension test for pantographic microstructures enables the simultaneous investigation of tensile, shear and bending effects [23]. This results from the fact that the loading direction is inclined rather than parallel to the orientation of the pantographic beams, as illustrated in Figure 3. The left edge was fully constrained while on the right side a displacement-controlled Dirichlet condition $\Delta_{u_{x_1}} \approx \frac{\mathbb{L}_2}{3}$ was imposed in the tensile-shear direction. This setup allowed microstructural kinematics to fully develop while avoiding locking, contact, and boundary artifacts. Under these conditions the pantographic metamaterial remained stable, i.e., no out-of-plane buckling occurred, and a series of experimental studies have confirmed the repeatability of the response.

Furthermore, the BIAS extension test provides direct reference data for the calibration of the energy density. These studies also contribute to advancing the understanding of pantographic microstructures by enabling the formulation of second-order models. Moreover, they provide experimental evidence that the macroscopic behavior of pantographic metamaterials is primarily governed by their microstructure [24]. Test with shear displacement imposed is illustrated in Figure 4. For a shear test, a Dirichlet displacement $\Delta_{u_{x_2}} \approx \frac{\mathbb{L}_2}{3}$ was imposed at the free edge while the left edge remained fully constrained. This test yields reference data for shear calibration for first and second-order models and for probing

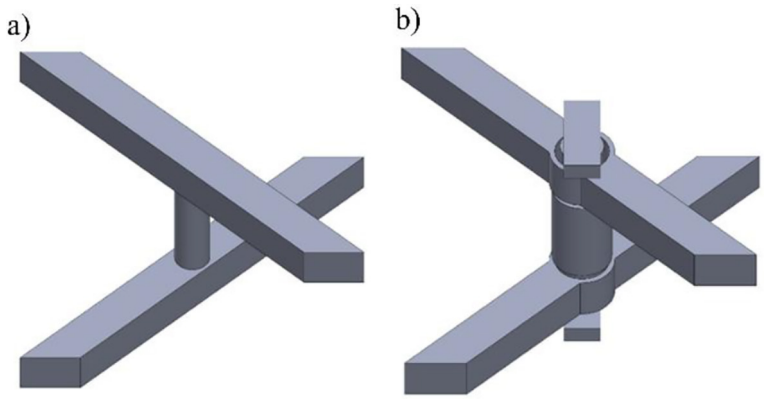

Figure 2. Type of pivots employed in pantographic metamaterial: (a) standard pivot and (b) quasi-perfect pivot

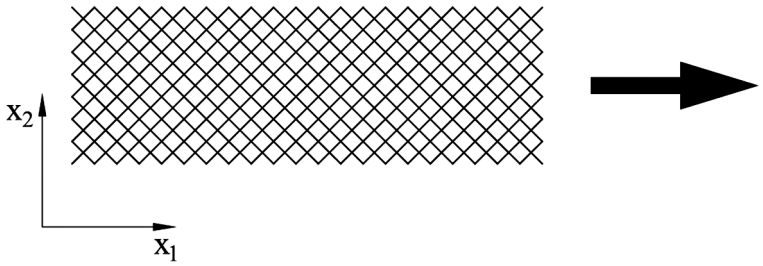

Figure 3. Load direction during BIAS extension test

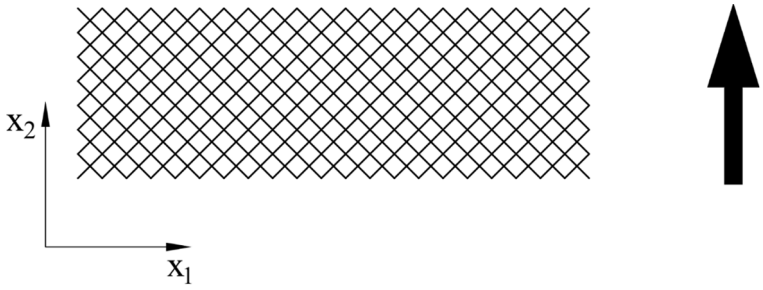

Figure 4. Load direction during shear test

instability thresholds [25,26]. Compared with BIAS extension, it enabled more direct identification of the shear stress-strain relationship because BIAS extension inherently produces a non-uniform shear field. Independently of the BIAS and shear tests, a case without external loads was considered, but with a predefined field of generalized forces applied at the hinges. A bending moment of M_{FZ} = -0.1 $N{\cdot}m$ was imposed on the translational-rotational springs. The purpose was to demonstrate in isolation that the pre-state alone could deform the microstructures and to investigate how it altered the energy distribution and the tangent stiffness of the system already in the initial equilibrium configuration.

Since the moment was self-equilibrated, the system reached equilibrium through beam deflection and axial and hinges rotation. The magnitude of the bending moment was deliberately chosen to be large in order to produce a clear and easily observable kinematic effort, and to serve as a diagnostic case for assessing the model's stability and the influence of the pre-state.

Optimization methodology

The optimization was carried out using a program written in C, which sequentially executed numerical simulations until the optimization criteria were satisfied or the convergence criterion, defined as the difference between consecutive iterations, was met. The next step, after selecting the model to represent pantographic metamaterial, was the formulation of the elastic energy functional of the structure. This functional describes the internal energy reduced by the work of the external loads, and its stationarity determines the equilibrium configuration. In the static analysis of a conservative system, equilibrium follows from the stationarity of the total potential energy:

$$\Pi = U_{int} - U_{ext}, \delta\Pi = 0 \qquad (2)$$

In case of pantographic structure modeled as a network of Euler-Bernoulli Beams connected by kinematic hinges reinforced with springs, the BIAS and shear test are formulated as the minimization of the internal energy subject to prescribed constraints. The boundary displacement on the right edge was imposed kinematically as a Dirichlet condition, and the corresponding reactions are obtained from the derivative of the energy with respect to imposed displacement.

Let $\mathbf{B} = \{1, 2, ..., N_b\}$ be the set of beams and $\mathbf{S} = \{1, 2, ..., N_s\}$ the set of translational-rotational springs connecting pairs of nodes. For each beam $j \in \mathbf{B}$ there is arc-length coordinates $s \in [0, L_j]$ along the beam centerline. The unit tangent to the deformed centerline defines the section rotation angle $\phi_j(s)$ with respect to the x-axis. The beam curvature is defined as $\kappa_j = \frac{d\phi_j}{ds}$, with the bending stiffness EI_j. The axial strain is given by

$\varepsilon_j = \frac{du_j}{ds}$, with the axial stiffness EA_j. For each spring $i \in \mathbf{S}$, let φ_i denote the rotational jump between its two nodes with rotational stiffness $k_{r,i}$. Accordingly, the total potential energy of system takes the form:

$$\Pi_{\text{BIAS,SHEAR}} = \sum_{i=1}^{N_s} \frac{1}{2} k_{r,i} \varphi_i^2 + \\ + \sum_{j=1}^{N_b} \int_0^{L_j} \left[\frac{1}{2} EI_j \kappa_j(s)^2 + \frac{1}{2} EA_j \varepsilon_j(s)^2 \right] ds \tag{3}$$

Pre-moment loading case contains the external work prescribed as a moment $M_{0,i}$ applied at each spring i of the structure. The total potential energy of the structure is:

$$\Pi_{\text{PRE}} = \sum_{i=1}^{N_s} \frac{1}{2} k_{r,i} \varphi_i^2 + \\ + \sum_{j=1}^{N_b} \int_0^{L_j} \left[\frac{1}{2} EI_j \kappa_j(s)^2 + \frac{1}{2} EA_j \varepsilon_j(s)^2 \right] ds - \\ - \sum_{i=1}^{N_s} M_{0,i} \varphi_i \tag{4}$$

Energy-equalizing spring stiffness optimization under BIAS and shear loading is performed with the following algorithm. At each iteration t, the structure is solved for the current stiffness set $\left\{k_{r,i}^{(t)}\right\}$, from which the mean energy is computed

$$\bar{U}^{(t)} = \frac{1}{N_s} \sum_{i=1}^{N_s} U_i^{(t)} \tag{5}$$

and the corresponding nondimensional deviations are subsequently evaluated

$$\delta_i^{(t)} = \frac{U_i^{(t)}}{\bar{U}^{(t)}} - 1 \tag{6}$$

The coefficient of variation is a dimensionless measure of dispersion of the elementwise energies around the mean. A decrease indicates progressive homogenization of the energy field and is calculated as

$$CV(U^t) = \frac{\sqrt{\frac{1}{N_s} \sum_{i=1}^{N_s} \left(U_i^{(t)} - \bar{U}^{(t)}\right)^2}}{\bar{U}^{(t)}} = \\ = \sqrt{\frac{1}{N_s} \sum_{i=1}^{N_s} \left(\delta_i^{(t)}\right)^2} \tag{7}$$

A logarithmic multiplicative update (exponentiated gradient) scheme is used to update the rotational stiffness. Springs with above-average energy are softened, while those with below-average energy are stiffened. The pre-projection multiplicative proposal is:

$$\tilde{k}_{r,i}^{(t+1)} = k_{r,i}^{(t)} e^{-\eta^{(t)} \delta_i^{(t)}} \tag{8}$$

The stepsize $\eta^{(t)}$ is chosen to be adapted to the data at each iteration so that the relative changes per spring remain limited. The trial stepsize η_0 is computed based on the maximum absolute value of the normalized deviations defined in Equation 6, and constrained by the relative change limit r_{max} leading to the expression:

$$\eta_0 = \frac{r_{max}}{\Delta}, where\ \Delta = max_i \left| \delta_i^{(t)} \right| \tag{9}$$

If $\Delta = 0$, a small positive fallback value is used to maintain numerical stability. Equation 9 ensures that the pre-projection log-increment satisfies the relative-change bound

$$\left| ln\left(\frac{\tilde{k}_{r,i}^{(t+1)}}{k_{r,i}^{(t)}} \right) \right| \leq r_{max} \tag{10}$$

During the optimization process, the relative-change limit was set to $r_{max} = 0.05$. Working in logarithmic space makes it possible to impose the bounds on relative changes directly via log-increments. For reference, $\ln(1.05) \approx 0.0488$, so the tolerance of r_{max} corresponds to a controlled stiffness variation of approximately ±5% per iteration. To prevent numerical overflow or underflow during exponential evaluation, the exponential $-\eta^{(t)}\delta_i^{(t)}$ is restricted to the range [−50,50], effectively limiting the magnitude of the multiplicative update. The update defined in Equation 8 is not accepted directly. Instead, it undergoes a projection step to enforce feasibility. The provisional field is projected onto the intersection of two constraints: per-element admissible stiffness range $[k_{r,min}, k_{r,max}]$ and the total stiffness sum constraint inherited from the previous iteration.

$$\bar{K} = \sum_{i=1}^{N_s} k_{r,i}^{(t)} \tag{11}$$

The global quantity defined in Equation 11 remained unchanged throughout the optimization process, ensuring that only a redistribution of stiffness occurs at each iteration. To simultaneously satisfy both constraints, a positive scaling

factor $s^{(t)} > 0$ is determined such that the scaled and bounded update from Equation 8 fulfills the admissibility conditions:

$$k_{r,i}^{(t+1)} = \min\left(\max\left(s^{(t)}\tilde{k}_{r,i}^{(t+1)}, k_{r,min}\right), k_{r,max}\right), \quad \bar{K} = \sum_{i=1}^{N_s} k_{r,i}^{(t+1)} \tag{12}$$

This projection step can be reformulated as solving a scalar equation for the scaling factor $s^{(t)}$ and leads to:

$$\Phi^{(t)}\left(s^{(t)}\right) = \sum_{i=1}^{N_s} \min\left(\max\left(s\tilde{k}_{r,i}^{(t+1)}, k_{r,min}\right), k_{r,max}\right) = \bar{K} \tag{13}$$

This Equation 13 mapping is continuous and nondecreasing, with boundary values $\Phi^{(t)}(0) = N_s k_{r,min}$ and if $s^{(t)} \to \infty$ then $\Phi^{(t)}(s^{(t)}) = N_s k_{r,max}$. The monotonic nature of the mapping $\Phi^{(t)}(s^{(t)})$ ensures that this solution is unique. The scaling factor $s^{(t)}$ is computed with the bisection method. After the projection step, an acceptance criterion is imposed. The Equation 8 is accepted only if the maximum relative change satisfies:

$$max_{i=1,\ldots,N_s}\left|ln\left(\frac{k_{r,i}^{(t+1)}}{k_{r,i}^{(t)}}\right)\right| \leq r_{max} \tag{14}$$

If the condition in Equation 14 is violated, the update is unacceptable. In such cases, the stepsize $\eta \leftarrow \eta/2$ and both the Equation 8 and projection step are recomputed. This backtracking strategy ensures numerical stability and promotes smooth convergence. The process of optimization terminated once the coefficients of variation Equation 7 fell below the threshold $\varepsilon_{CV} = 0.07$ for $p = 2$ consecutive iterations, provided that the iteration count exceeds $t_0 = 2$. This prevents premature termination and confirms that the energy field has sufficiently stabilized. This condition $CV(U^t) < \varepsilon_{CV}$ indicates that the stored potential energy is nearly evenly spread across the lattice, ensuring that no subset of spring is overstressed or underutilized. The condition that total stiffness sum remains fixed throughout the optimization process causes only a redistribution occurs without altering the global load-displacement response of the structure. All necessary parameters for conducting the simulation and optimization, as well as model-related information, are provided in Table 2.

RESULTS

Unoptimized and optimized microstructures are compared for two loading cases, BIAS extension and shear, each evaluated at three lattice

Table 2. Numerical parameters

Category	Parameter	Value/Range	Unit
Geometry	Cells along $\mathbb{L}_1$	7,10,14	-
	Cells along $\mathbb{L}_2$	21,30,42	-
	Number of springs	319, 637, 1229	-
	Length of shorter side $\mathbb{L}_1$	0.07	m
	Length of longer side $\mathbb{L}_2$	0.21	m
	Beam cross-section	1×10^{-6}	m^2
Material properties	Young's modulus	1650	MPa
	Poisson's ratio	0.3	-
	Translation stiffness	1×10^{-9}	$N \cdot m^{-1}$
	Rotational stiffness	2.5519×10^{-2}	$N \cdot m \cdot rad^{-1}$
	Rotational stiffness range	6.23×10^{-6} – 6.23×10^{-2}	$N \cdot m \cdot rad^{-1}$
Boundary conditions	BIAS displacement	$\Delta_{ux1} \approx \mathbb{L}_1/3$	m
	Shear test displacement	$\Delta_{ux2} \approx \mathbb{L}_2/3$	m
	Pre-moment case	$M_{FZ} = -0.1$	N·m
Optimization settings	Maximum iterations	500	–
	Convergence threshold	0.07	–
	Relative change limit	0.05 (≈ ±5%)	–
	Consecutive passes	2	–
	Min. iterations before CV	2	–

resolutions. The von Mises stress field for the BIAS extension test is presented first, along with the corresponding spring-energy maps, followed by the optimized stiffness fields. The same sequence is applied to the shear test. The pre-moment case is addressed subsequently. A pre-moment configuration is shown qualitatively. Only deformed geometry and energy maps are reported. Quantitative summaries, including peak von Mises stress, maximum spring energy, and reduction factors, are provided in Table 3 and Table 5, while active set analyses of energy homogenization based on the 10th percentile threshold ($\tau_{0.1}$) are reported in Table 4 and Table 6.

Numerical results

Under the BIAS extension test, the pantographic structure exhibits the canonical mixed bending-tension response with a central necking and boundary layers near the clamp. In the unoptimized configurations (Figure 5a,c,e), the peak von Mises stress increases with microstructural density N_f. This is a consequence of a larger number of pivots, which favor the localization of deformation on the neck and the accumulation of energy. After optimization (Figure 5b,d,f), the structure finds a new kinematically admissible minimum, which develops a thin, well-defined central neck. The maximum von Mises stress consistently stabilizes at approximately 5×10^7 Pa irrespective of N_f. The optimization procedure preserves the global force-displacement response, suggesting that stiffness redistribution does not affect macroscopic behavior. Figure 6 illustrates the influence of energy equalization on the redistribution of local work within the pantographic lattice under BIAS. In the baseline configuration (Figure 6a,c,e), spring potential energy is concentrated in the central neck region. Boundary layers and corners zones exhibit minimal energy accumulation. Consequently, the energy input is unevenly distributed, with the central pivots in the neck region accounting for a dominant share of the total work. In contrast, the optimized configuration (Figure 6b,d,f) exhibits a nearly homogeneous distribution of spring potential energy across the active domain. This corresponds to a significant attenuation of local energy peaks compared to the initial configuration. A coherent field of spring potential energy develops, spanning the majority of the pantographic lattice. Energetically subdued regions persist near the clamps and corners. This is a direct consequence of Dirichlet boundary conditions that suppress local rotations. Nevertheless, the optimization procedure ensures a high degree of uniformity in regions free from such constraints, underscoring the effectiveness in mitigating local disparities wherever boundary effects do not interfere.

Figure 7 illustrates the final rotational stiffness field together with its increment relative to the initial state, $\Delta k_r = k_r^{500} - k_r^0$, exposing how the energy equalization procedure redistributes

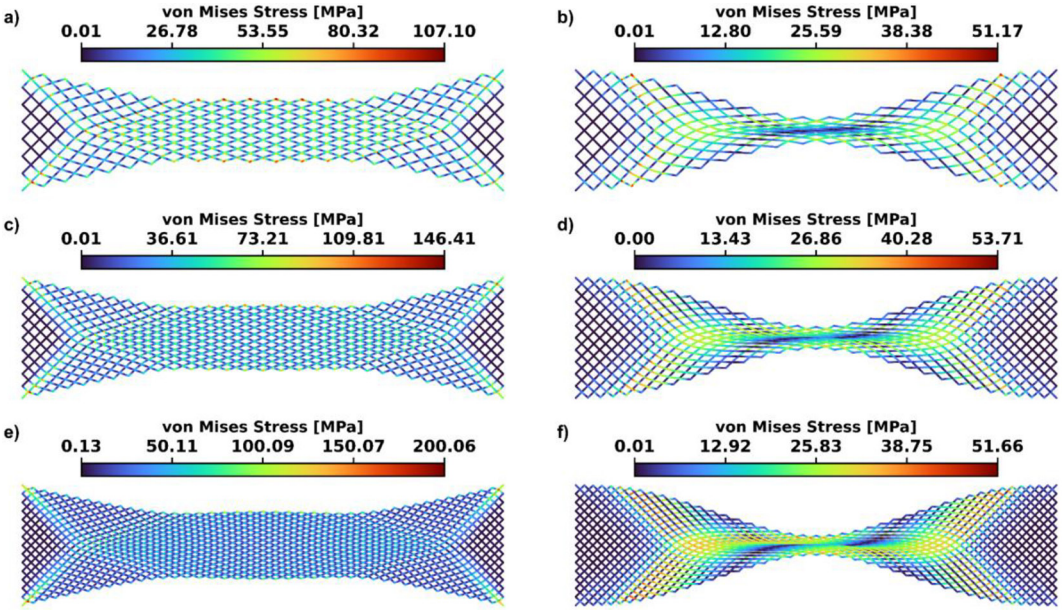

Figure 5. von Mises equivalent stress for the BIAS extension test: (a, c, e) – unoptimized structures, (b, d, f) – optimized structures after energy equalization. Rows N_f = 7, 10, 14

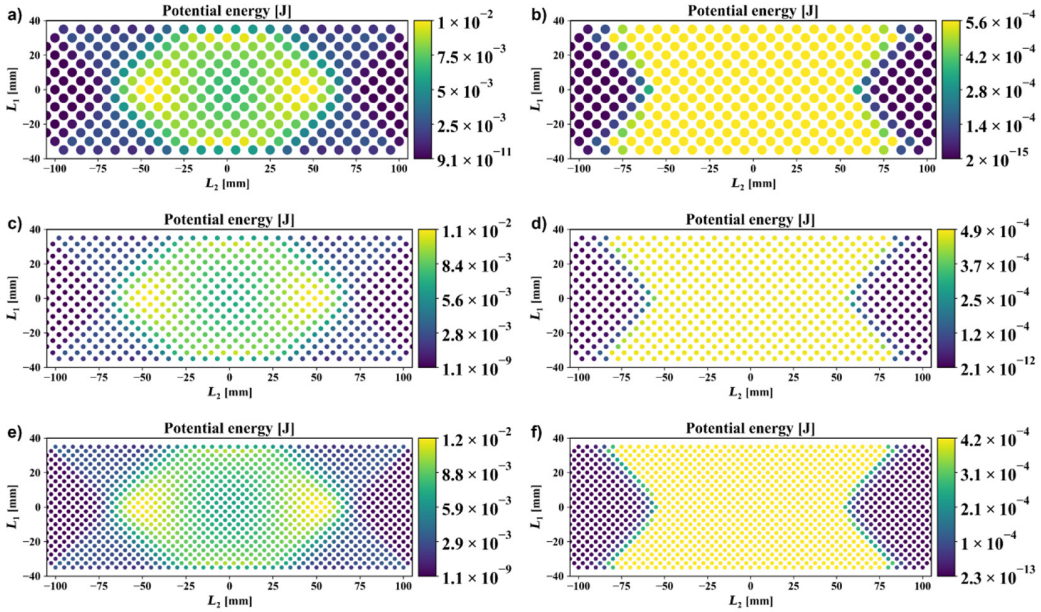

Figure 6. Potential energy stored in the springs of a pantographic lattice for the BIAS extension test: (a, c, e) – unoptimized structures, (b, d, f) – optimized structures after energy equalization. Rows Nf = 7, 10, 14

mechanical penalties across the pantographic lattice under a fixed global quantity Equation 11. The center is systematically softened, while the near-clamp regions are driven toward the upper bound of the maximum admissible stiffness. This configuration facilitates the emergence of a narrow kinematic waist seen in Figure 5b, d and f.

Before optimization, the neck region concentrates the majority of springs work. Consequently, the algorithm selectively reduces the stiffness in this area until its energy contribution aligns with the lattice-wide average, thereby equalizing the distribution of mechanical effort. The neck does not collapse to $k_{r,min}$ either, because the objective was to equalize energies rather than to minimize k_r locally. In contrast, the outer regions contribute insufficient mechanical work and are therefore selectively stiffened to enhance their role on load transmission. This pattern is consistently preserved across all three configurations N_f = 7, 10, 14, regardless of lattice refinement. The outcomes of the optimization process for the BIAS

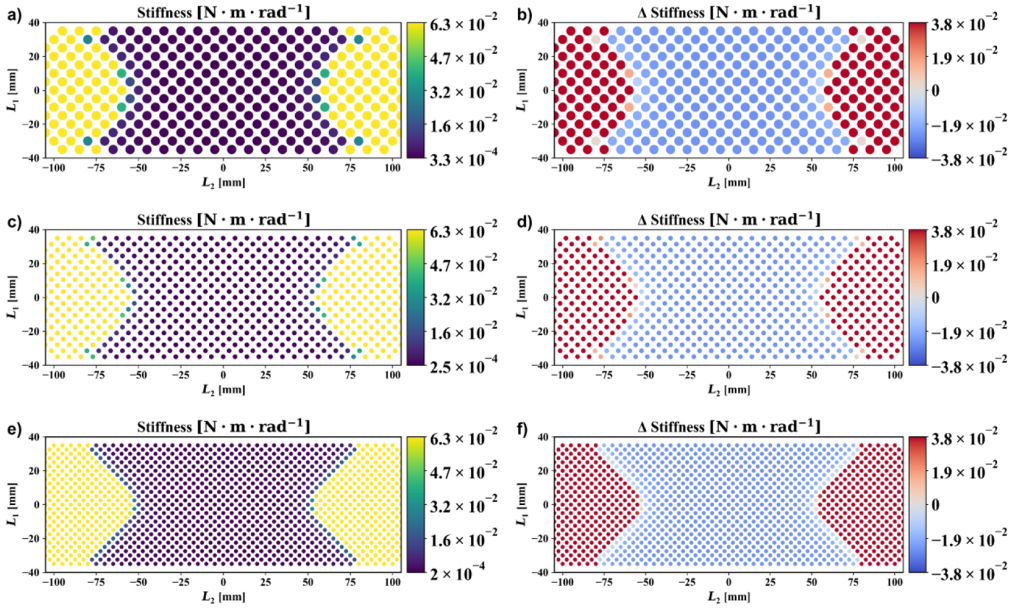

Figure 7. Spring rotational stiffness in a pantographic lattice for the BIAS extension test and its difference relative to the initial state: (a, c, e) – optimized structures k_r^{500}, (b, d, f) – $\Delta k_r = k_r^{500} - k_r^0$. Rows N_f = 7, 10, 14

are summarized in Table 3, reporting the peak von Mises stress, the maximum spring energy and the corresponding reduction factors for all cases.

To quantify the homogenization on load-carrying pivots, $CV(U^t)$ was additionally evaluated on active set defined by a 10th percentile threshold on the combined energy distribution. A pivot is marked active if $U_i^t > \tau$ in either state. Negative ΔCV indicates improved energy homogenization. The minor change at $N_f = 14$ is consistent with the larger fraction of pivots adjacent to the clamp and bound-active constraints rather than by a lack of convergence. These results are illustrated in Table 4.

Under shear loading, the pantographic lattice forms two families of rhombi that rotate in opposite directions and a diagonal load path. In the unoptimized configurations (Figure 8a,c,e) the von Mises stress assembles into oblique bands aligned with the principal shear directions. After optimization (Figure 8b,d,f) the pantographic structure adopts a new kinematically admissible deformation mode in which the diagonal shear band is clearer and more coherent. The von Mises stress peaks are capped and exhibit markedly reduced sensitivity to N_f. Spatially, stress concentrations remain on the shear paths, but their distribution becomes more uniform. Figure 9 illustrates the distribution of local spring potential energy in the pantographic lattice under shear loading. In the initial state (Figure 9a,c,e), the field exhibits a fragmented distribution. Peak values appear near the narrows while the diagonal load path remains relatively under-energized. Only a small part of all pivots absorbs a disproportionately large share of the work. After optimization (Figure 9b,d,f) the field assumes a spatially uniform profile across the active domain, indicative of a homogenized mechanical response. A diamond-like region of low energy persists at the intersection of the principal shear directions. Meanwhile, previously underutilized regions are activated to share mechanical effort more evenly. As N_f increases, the optimized field exhibits enhanced smoothness and the residual diagonal fades.

Figure 10 makes the mechanism explicit. In the response to shear loading, the optimized stiffness distribution assembles into a diamond-shaped interior skeleton aligned with the principal shear directions, bordered by softened outer regions (Figure 10a,c,e) that facilitate broader deformation. As the lattice is refined this diamond structure preserves its connectivity. Pivots situated along the principal shear diagonals approach $k_{r,max}$, reinforcing the integrity of the oblique deformation mode. The distribution Δk_r (Figure 10b,d,f) exhibits positive bands along those diagonals and negative belts near the structural boundaries. The optimized structure reinforces the spring centrally, enhancing the oblique deformation mode while it preserves connectivity across all configurations N_f. Table 5 summarizes the results of the optimization process for the shear test, including the peak von Mises stress, the maximum spring energy, and the associated reduction factors for each configuration.

Under the shear loading, the optimization yields strong energy equalizations across all refinements. On the active set defined by 10th percentile threshold ($\tau_{0.1}$), $CV(U^t)$ decreases markedly indicating efficient homogenization among load-carrying pivots. The consistent drop $\Delta CV(U^t) \approx$ -0.6 across all configurations of lattice confirms the robustness of optimization with respect to lattice refinement. Table 6 presents this consistency.

Applying a uniform field of a bending moment of M_{FZ} to the springs in the hinges leads

Table 3. Quantitative synthesis of the BIAS extension test

N_f	$\sigma_{VM}^{max(unopt)}$	$\sigma_{VM}^{max(opt)}$	Reduction (x)	$U_{max}^{(unopt)}$	$U_{max}^{(opt)}$	Reduction (x)
7	107.1 MPa	51.2 MPa	~2.1x	1.0×10^{-2} J	5.6×10^{-4} J	~17.9x
10	146.4 MPa	53.7 MPa	~2.7x	1.1×10^{-2} J	4.9×10^{-4} J	~22.4x
14	200.0 MPa	51.7 MPa	~3.9x	1.2×10^{-2} J	4.2×10^{-4} J	~28.6x

Table 4. Active set analysis of energy homogenization in the BIAS extension test

N_f	Springs	Active	$\tau_{0.1}$	$CV(U^t)_{unopt}$	$CV(U^t)_{unopt}$	$\Delta CV(U^t)$
7	319	92.2 %	2.27×10^{-7} J	0.662	0.519	-0.143
10	637	92.8 %	7.41 × 10-8 J	0.625	0.557	-0.068
14	1229	94.3 %	4.68×10^{-7} J	0.607	0.608	+0.001

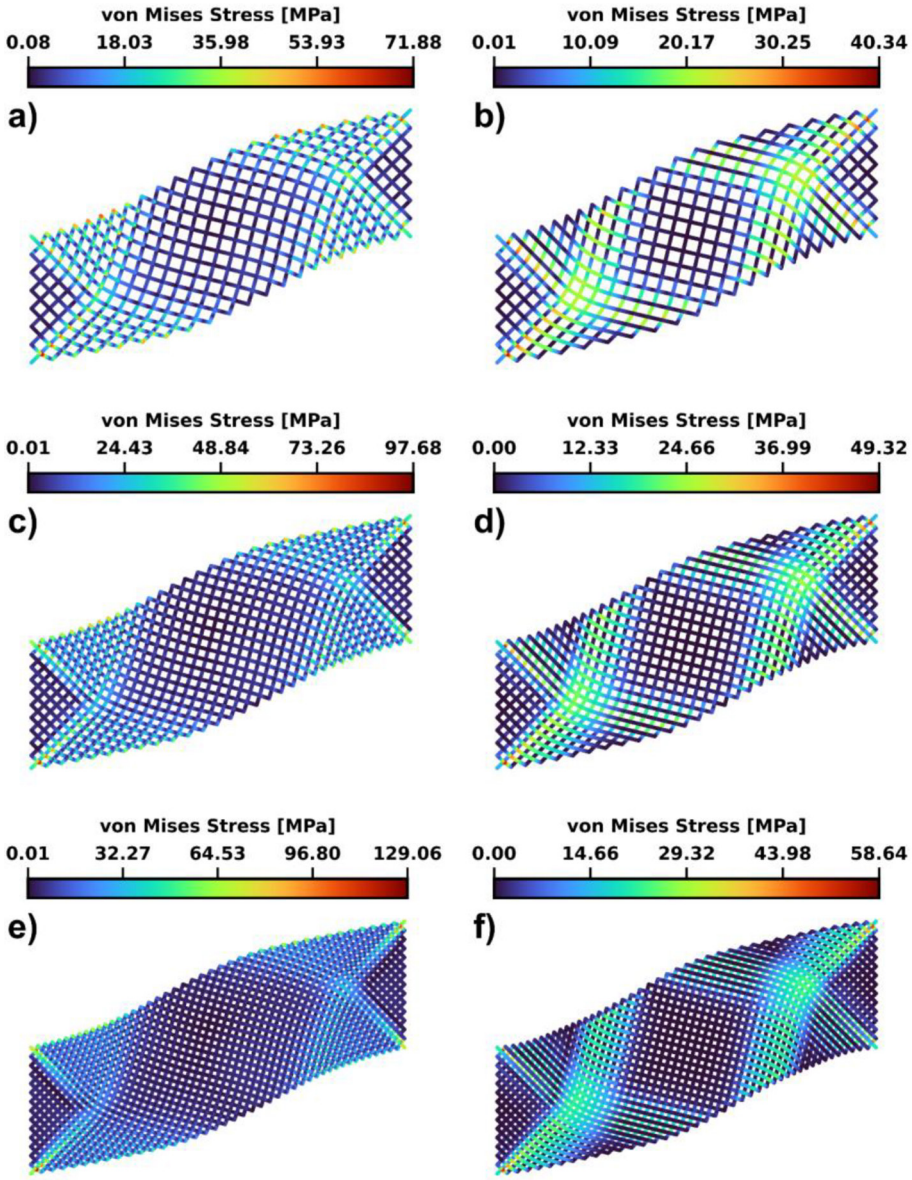

Figure 8. von Mises equivalent stress in a pantographic lattice for the shear test: (a, c, e) – unoptimized structures, (b, d, f) – optimized structures after energy equalization. Rows N_f = 7, 10, 14

Table 5. Quantitative synthesis of the shear test

N_f	$\sigma_{VM}^{max(unopt)}$	$\sigma_{VM}^{max(opt)}$	Reduction (x)	$U_{max}^{(unopt)}$	$U_{max}^{(opt)}$	Reduction (x)
7	71.9 MPa	40.3 MPa	~1.8x	2.9×10^{-3} J	4.5×10^{-5} J	~64.4x
10	97.7 MPa	49.3 MPa	~2.0x	3.1×10^{-3} J	4.1×10^{-5} J	~75.6x
14	129.1 MPa	58.6 MPa	~2.2x	3.2×10^{-3} J	2.5×10^{-5} J	~128.0x

to equilibrium achieved solely through the rotational displacement. The mechanical deformation of lattice arises from kinematic coupling between adjacent unit cells and the absence of external constraint. At the edges of the structure, where applied field cannot be balanced internally, the network undergoes global outward deformation, resulting in a visible increase in projected width (Figure 11a,c,e). Peak energy values are concentrated on the edge of lattice, indicating that the structural work is primarily absorbed by the first rows of unit cells. Figure 11b, d, and f illustrates as the microstructural density N_f increases, the same deformation effect is distributed across a greater number of unit cells, thereby reducing the energy per spring.

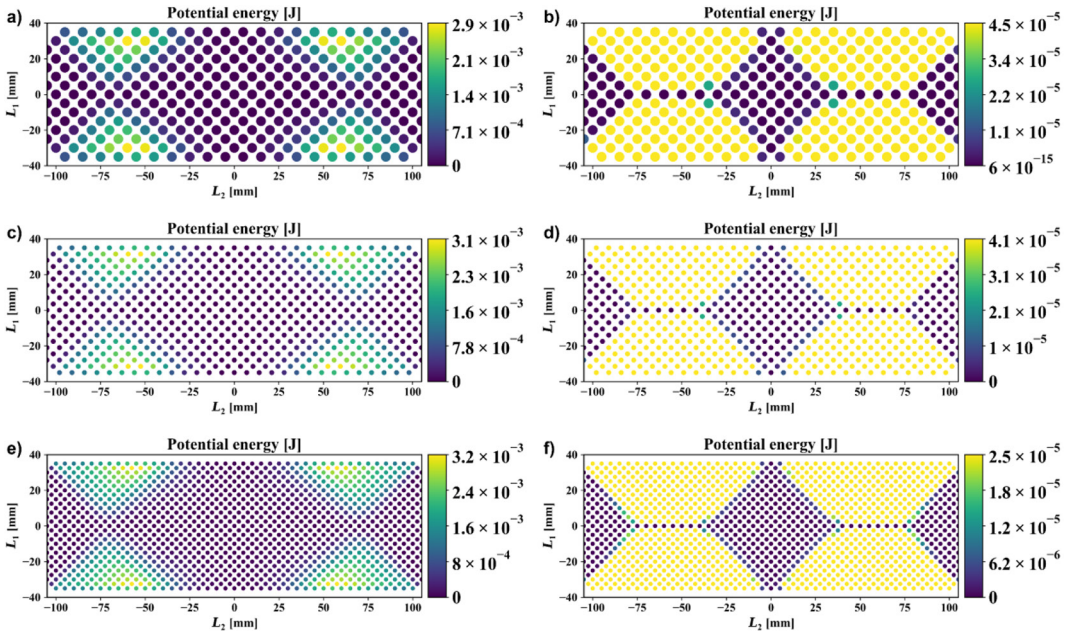

Figure 9. Potential energy stored in the springs of a pantographic lattice for the shear test: (a, c, e) – unoptimized structures, (b, d, f) – optimized structures after energy equalization. Rows $N_f = 7, 10, 14$

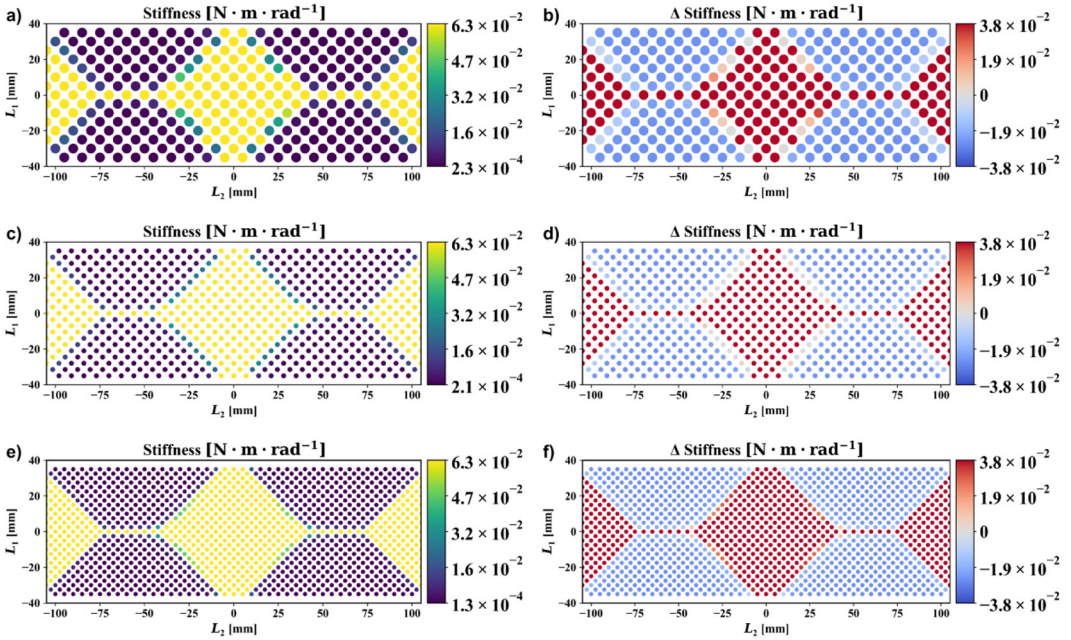

Figure 10. Spring rotational stiffness in a pantographic lattice for the shear test and difference relative to the initial state: (a, c, e) – optimized structures k_r^{500}, (b, d, f) – $\Delta k_r = k_r^{500} - k_r^0$. Rows $N_f = 7, 10, 14$

DISCUSSION

In this study, a complementary strategy for controlling behavior in a pantographic lattice is proposed, based on discrete optimization of local stiffness rather than the reformulation of the continuum model. The present results are consistent with established theoretical and experimental framework, particularly in terms of observed kinematic patterns for the unoptimized lattice [18]. Extensive studies have demonstrated that pantographic metamaterials homogenize into second-gradient continuum models, which accurately reproduce characteristic responses such as necking and oblique shear band formation under BIAS and shear loading [27,28]. The main result of the conducted research is the demonstration that balancing the spring energy

Table 6. Active set analysis of energy homogenization in the shear test

N_f	Springs	Active	$\tau_{0.1}$	$CV(U^t)_{unopt}$	$CV(U^t)_{opt}$	$CV(U^t)$
7	319	92.5 %	4.18×10^{-9} J	1.214	0.574	-0.640
10	637	92.3 %	1.18×10^{-8} J	1.208	0.603	-0.605
14	1229	94.2 %	2.03×10^{-8} J	1.226	0.610	-0.616

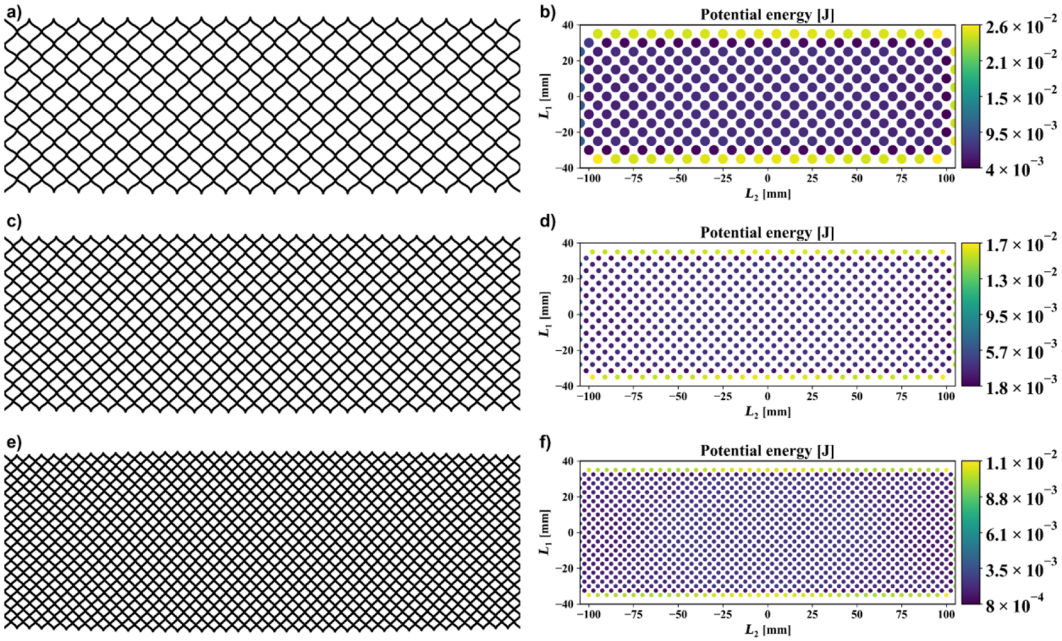

Figure 11. Pre-moment state: (a, c, e) – deformed configuration, (b, d, f) – potential energy stored in the springs of a pantographic lattice. Rows N_f = 7, 10, 14

by modifying the rotational stiffness of the pivots while maintaining a constant total stiffness and adhering to predefined lower and upper constraints leads to flattening of the operating fields, reducing the von Mises stress, and stabilizing the macroscopic response of the lattice. These effects were observed in the three distinct loading cases, including the BIAS extension test, the shear loading and the configuration involving a pre-applied bending moment field. The observed kinematic and energy patterns align with mechanics of pantographic metamaterial and second-gradient theories [29,30], which predict localization regularization and field smoothing through microstructural kinematic penalties. The results confirm that appropriately distributed rotational stiffness can act as a mechanism for controlling energy localization and enhancing structural response stability in material with tunable microarchitectures. Under the BIAS extension test, the optimization alleviates stress concentrations in the neck region by locally reducing rotational stiffness and assigning near-maximal stiffness near the clamps, effectively broadening the load path, and suppressing peak stresses. Under the shear test, the optimized configuration promotes a diamond-like interior skeleton with softened outer margins of the lattice. This structural adaptation reorganizes load transmission along oblique principal directions. Its internal architecture is adapted to better accommodate shear forces. Under the pre-applied bending moment field configuration, purely kinematic coupling is activated, producing edge-dominated energy uptake and an anisotropic pre-shape that biases subsequent deformation. This capability allows directional control of energy flow to relative external loading and highlights the role of pre-stressed states in tailoring the response of programmable metamaterials. From an algorithmic standpoint, the multiplicative log-update mechanism decreases stiffness in regions where mechanical work exceeds the average and increases it where stiffness is under-utilized. The projection step ensures feasibility. Meanwhile, the coefficient of variation $CV(U^t)$ emerges as

a robust convergence metric, capturing the uniformity of the energy distribution across the lattice. Prior optimization efforts on pantographic lattices have primarily focused on tuning macroscopic shear-stiffness fields or continuum parameters to extend elastic range or delay rupture, typically formulated at the homogenized or coarse-grained level [31]. In contrast, the present approach operates directly at the lattice scale, yielding outcomes that are not targeted in macro-level optimization studies. By acting on discrete elements, the method complements and extends recent research emphasizing the role of energy-driven, adaptive redistribution across the lattice. The observed effects not only validate the effectiveness of discrete stiffness redistribution in pantographic lattices but also reveal a broader potential for programmable control, enhanced durability, and multi-scale integration, setting the stage for future developments. Discrete stiffness equalization transcends conventional static field regularization by establishing the groundwork for lifetime-aware control strategies in pantographic lattices. A crucial next step is to extend the pivot formulation by incorporating damage, plasticity, and friction effects at the rotational interface. Such enhancements would enable rigorous quantification of how optimized stiffness distribution mitigates fatigue by delaying initiation and slowing accumulation. This advancement would transform the method from a purely kinematic smoothing tool into a microstructural controller capable of managing long-term degradation.

Although the present study focuses on computational optimization, the obtained stiffness redistribution patterns are directly compatible with existing additive manufacturing methods such as selective laser sintering or fused filament fabrication. The optimized geometries can be fabricated using polymeric or metallic filament with adjustable pivot stiffness allowing controlled replication. This provides a direct bridge from the proposed stiffness redistribution to experimentally verifiable, manufacturable pantographic metamaterials. An additional perspective involves temporal modulation of stiffness fields, where individual pivots undergo controlled stiffness decay over time. Such 4D behavior, characterized by dynamically evolving mechanical properties, could be programmed to maintain uniform energy distribution or control deformation paths in response to changing loads. The lattice becomes capable of adapting its internal microstructures in real time, effectively embedding chronologically tunable response into the material system. Altogether, the study suggests that discrete stiffness equalization is a promising and physically grounded strategy with potential to enhance mechanical durability, adaptability, and fatigue resistance in the pantographic lattice.

CONCLUSIONS

The study presents a framework for optimizing the microstructure of pantographic metamaterial by modeling pivots as kinematic hinges complemented by coupled translational-rotational springs, with total stiffness conserved. Across the two loading scenarios and three lattice resolutions refinements, the procedure homogenizes spring-energy fields, reduces peak von Mises stresses. The deformation patterns align with pantographic mechanics, including narrowing of the critical zone in the BIAS extension test, internal skeleton formation under shear loading and energy localized absorption during pre-moment loading. These results indicate that stiffness equalization of the pivots provides a straightforward route to reduce stress concentration and stabilize macroscopic behavior without changes to material or overall geometry.

REFERENCES

1. Walser RM. Metamaterials: What are they? What are they good for? APS March Meeting Abstracts, 2000; 5: 1.
2. Bilotti F, Sevgi L. Metamaterials: Definitions, properties, applications, and FDTD-based modeling and simulation. International Journal of RF and Microwave Computer-Aided Engineering 2012;22:422–38.
3. Lapine M, Tretyakov S. Contemporary notes on metamaterials. IET Microw Antennas Propag 2007;1:3–11. https://doi.org/10.1049/iet-map:20050307
4. Kumar R, Kumar M, Chohan JS, Kumar S. Overview on metamaterial: History, types and applications. Materials Today: Proceedings 2022;56:3016–24. https://doi.org/10.1016/j.matpr.2021.11.423
5. Wang Y-F, Wang Y-Z, Wu B, Chen W, Wang Y-S. Tunable and Active Phononic Crystals and Metamaterials. Applied Mechanics Reviews 2020;72:040801. https://doi.org/10.1115/1.4046222.
6. Ju J, Gao X-L. Mechanical Metamaterials:

Cutting-Edge Metastructures. vol. 8. Frontiers Media SA; 2022.

7. dell'Isola F, Steigmann D, Corte AD. Synthesis of fibrous complex structures: designing microstructure to deliver targeted macroscale response. Applied Mechanics Reviews 2015;67:060804. https://doi.org/10.1115/1.4032206
8. Abdoul-Anziz H, Seppecher P. Strain gradient and generalized continua obtained by homogenizing frame lattices. Math Mech Compl Sys 2018;6:213–50. https://doi.org/10.2140/memocs.2018.6.213
9. Madeo A, Della Corte A, Greco L, Neff P. Wave propagation in pantographic 2D lattices with internal discontinuities. Proc Estonian Acad Sci 2015;64:325. https://doi.org/10.3176/proc.2015.3S.01
10. dell'Isola F, Lekszycki T, Pawlikowski M, Grygoruk R, Greco L. Designing a light fabric metamaterial being highly macroscopically tough under directional extension: first experimental evidence. Z Angew Math Phys 2015;66:3473–98. https://doi.org/10.1007/s00033-015-0556-4
11. Valipour A, Kargozarfard MH, Rakhshi M, Yaghootian A, Sedighi HM. Metamaterials and their applications: An overview. Proceedings of the Institution of Mechanical Engineers, Part L: Journal of Materials: Design and Applications 2022;236:2171–210. https://doi.org/10.1177/1464420721995858
12. dell'Isola F, Seppecher P, Alibert JJ, Lekszycki T, Grygoruk R, Pawlikowski M, et al. Pantographic metamaterials: an example of mathematically driven design and of its technological challenges. Continuum Mech Thermodyn 2019;31:851–84. https://doi.org/10.1007/s00161-018-0689-8
13. Laudato M, Di Cosmo F, Drobnicki R, Göransson P. Dynamical Vector Fields on Pantographic Sheet: Experimental Observations. In: Abali BE, Altenbach H, dell'Isola F, Eremeyev VA, Öchsner A, editors. New Achievements in Continuum Mechanics and Thermodynamics, vol. 108, Cham: Springer International Publishing; 2019;257–69. https://doi.org/10.1007/978-3-030-13307-8_19
14. Alibert J-J, Seppecher P, Dell'Isola F. Truss Modular Beams with Deformation Energy Depending on Higher Displacement Gradients. Mathematics and Mechanics of Solids 2003;8:51–73. https://doi.org/10.1177/1081286503008001658
15. dell'Isola F, Steigmann DJ, editors. Discrete and Continuum Models for Complex Metamaterials. 1st ed. Cambridge University Press; 2020. https://doi.org/10.1017/9781316104262
16. Andreaus U, Spagnuolo M, Lekszycki T, Eugster SR. A Ritz approach for the static analysis of planar pantographic structures modeled with nonlinear Euler–Bernoulli beams. Continuum Mech Thermodyn 2018;30:1103–23. https://doi.org/10.1007/s00161-018-0665-3
17. dell'Isola F, Giorgio I, Pawlikowski M, Rizzi NL. Large deformations of planar extensible beams and pantographic lattices: heuristic homogenization, experimental and numerical examples of equilibrium. Proc R Soc A 2016;472:20150790. https://doi.org/10.1098/rspa.2015.0790
18. dell'Isola F, Seppecher P, Spagnuolo M, Barchiesi E, Hild F, Lekszycki T, et al. Advances in pantographic structures: design, manufacturing, models, experiments and image analyses. Continuum Mechanics and Thermodynamics 2019;31:1231–82
19. Shekarchizadeh N, Abali BE, Barchiesi E, Bersani AM. Inverse analysis of metamaterials and parameter determination by means of an automatized optimization problem. Z Angew Math Mech 2021;101:e202000277. https://doi.org/10.1002/zamm.202000277
20. Barchiesi E, Eugster SR, Placidi L, dell'Isola F. Pantographic beam: a complete second gradient 1D-continuum in plane. Z Angew Math Phys 2019;70:135. https://doi.org/10.1007/s00033-019-1181-4
21. Rosi G, Auffray N. Anisotropic and dispersive wave propagation within strain-gradient framework. Wave Motion 2016;63:120–34. https://doi.org/10.1016/j.wavemoti.2016.01.009
22. Yildizdag ME, Ciallella A, D'Ovidio G. Investigating wave transmission and reflection phenomena in pantographic lattices using a second-gradient continuum model. Mathematics and Mechanics of Solids 2023;28:1776–89. https://doi.org/10.1177/10812865221136250
23. dell'Isola F, Della Corte A, Greco L, Luongo A. Plane bias extension test for a continuum with two inextensible families of fibers: A variational treatment with Lagrange multipliers and a perturbation solution. International Journal of Solids and Structures 2016;81:1–12. https://doi.org/10.1016/j.ijsolstr.2015.08.029
24. Barchiesi E, dell'Isola F, Hild F. On the validation of homogenized modeling for bi-pantographic metamaterials via digital image correlation. International Journal of Solids and Structures 2021;208–209:49–62. https://doi.org/10.1016/j.ijsolstr.2020.09.036
25. Scerrato D, Giorgio I, Rizzi NL. Three-dimensional instabilities of pantographic sheets with parabolic lattices: numerical investigations. Z Angew Math Phys 2016;67:53. https://doi.org/10.1007/s00033-016-0650-2
26. Barchiesi E, Ganzosch G, Liebold C, Placidi L, Grygoruk R, Müller WH. Out-of-plane buckling of pantographic fabrics in displacement-controlled shear tests: experimental results and model validation. Continuum Mech Thermodyn 2019;31:33–45. https://doi.org/10.1007/s00161-018-0626-x
27. Giorgio I, Della Corte A, dell'Isola F, Steigmann DJ. Buckling modes in pantographic lattices. Comptes Rendus Mécanique 2016;344:487–501. https://doi.

org/10.1016/j.crme.2016.02.009

28. Harrison P, Taylor E, Alsayednoor J. Improving the accuracy of the uniaxial bias extension test on engineering fabrics using a simple wrinkle mitigation technique. Composites Part A: Applied Science and Manufacturing 2018;108:53–61. https://doi.org/10.1016/j.compositesa.2018.02.025
29. Coutris N, Thompson LL, Kosaraju S. Asymptotic homogenization models for pantographic lattices with variable order rotational resistance at pivots. Journal of the Mechanics and Physics of Solids 2020;134:103718. https://doi.org/10.1016/j.jmps.2019.103718
30. Turco E, Barcz K, Pawlikowski M, Rizzi NL. Non-standard coupled extensional and bending bias tests for planar pantographic lattices. Part I: numerical simulations. Z Angew Math Phys 2016;67:122. https://doi.org/10.1007/s00033-016-0713-4
31. Desmorat B, Spagnuolo M, Turco E. Stiffness optimization in nonlinear pantographic structures. Mathematics and Mechanics of Solids 2020;25:2252–62. https://doi.org/10.1177/1081286520935503